
QUIET SOLAR CORONA: DAILY IMAGES AT 8.8–10.7 cm WAVELENGTHS

A.T. Altyntsev

*Institute of Solar-Terrestrial Physics SB RAS,
Irkutsk, Russia, altyntsev@iszf.irk.ru*

M.V. Globa

*Institute of Solar-Terrestrial Physics SB RAS,
Irkutsk, Russia, globa@iszf.irk.ru*

N.S. Meshalkina

*Institute of Solar-Terrestrial Physics SB RAS,
Irkutsk, Russia, nata@iszf.irk.ru*

Abstract. We discuss results of test observations of the 3–6 GHz range array of the Siberian Radio Heliograph (SRH). A method for calibrating brightness temperatures of images was verified using measurements of the brightness temperature of the quiet Sun at a minimum between solar activity cycles 20 and 21 known in the literature. The obtained time dependences of the integral solar flux at 2.8 GHz are similar to those measured at the Dominion Radio Astrophysical Observatory (DRAO), but the absolute values of SRH fluxes are lower relative to the DRAO fluxes by 10–15 %.

The spectral density of the solar microwave flux at a frequency of 2.8 GHz, the so-called $F10.7$ index, is one of the main solar activity indices used as input parameters in models of Earth's ionosphere. The paper considers the relationship between total radio fluxes and changes in the structure of sources on the solar disk during an interval of 50 days. During the period of daily observations from September 1 to October 20, 2021, the number of active regions on the disk changed several

times, and the integral flux density at 2.8 GHz changed up to 1.5 times. We determine the relative contributions to the integral flux of bremsstrahlung of near-limb brightenings and plage regions, as well as bremsstrahlung in magnetic fields of active regions. The measured brightness temperatures of SRH radio maps are compared to the model temperatures calculated from observations of extreme ultraviolet emission (EUV) with the AIA/SDO telescope. The results of the analysis can be used to organize regular measurements of the corrected solar activity proxy index $F10.7$ at SRH, in which the contribution of gyroresonance emission is excluded.

Keywords: total solar flux, $F10.7$ index.

INTRODUCTION

UHF observations of solar radio flux are most demanded in solar-terrestrial physics. This is due to the fact that properties of Earth's upper atmosphere (ionosphere—thermosphere) depend significantly on the high-energy flux of extreme ultraviolet emission from the Sun (EUV emission, 100–1210 Å) and even on the shorter-wavelength emission generated in the solar atmosphere. EUV emission heats and ionizes Earth's atmosphere, but does not reach its surface. Since it is impossible to detect EUV emission by ground-based instruments, the spectral density of the quiet Sun's emission flux at a frequency of 2.8 GHz, for which Earth's atmosphere is almost transparent, is used to estimate its flux. The high correlation between the microwave flux and the EUV emission intensity makes it possible to use it as a proxy index of solar activity, known as the $F10.7$ index. The high correlation between the index and the solar EUV emission is physically due to the generation of both emissions in the same coronal plasma [Swarup et al., 1963]. The index is taken to be equal to the spectral flux density of the quiet (time intervals without flares) solar emission measured on Earth at 2.8 GHz in solar flux units [10^{-22} W/(m²Hz)]. As reference, measurements of $F10.7$ from Canadian observatories are used; at these observatories, the accuracy of absolute

measurements is ~1 %; the measurements have been complemented daily from 1947 to the present day [Covington, 1969; Tapping, 1987]. This index is the main input parameter in up-to-date models of the ionosphere and thermosphere [Jacchia, 1971; Bilitza, Reinisch, 2008] even if direct EUV observations are available [Tobiska et al., 2008].

It is known (see reviews [Kundu, 1965; Krueger, 1979]) that thermal sources of microwave emission from the quiet Sun can be divided into three classes: background emission from the chromosphere and the overlying corona, moderate-intensity emission from plage regions, and bright emission from sunspots of active regions. The most accurate measurements of the brightness temperature spectrum in the center of the solar disk were carried out at the solar minimum between solar cycles 21 and 22 (1986–1987) and were published in [Zirin et al., 1991; Borovik et al., 1992]. The quiet Sun's brightness temperature at 2.8 GHz was defined as $(27.1 \pm 1.1)10^3$ K. The background component (65.2 ± 2.0 sfu) was shown to be generated in the homogeneous optically thick chromosphere with a temperature of 11000 K and in the overlying optically thin corona with a temperature of $\sim 10^6$ K.

Questions about the relative contribution of other sources to the $F10.7$ variability are still under discussion [Schonfeld et al., 2017]. Some studies claim that the

variable microwave component is an optically thin bremsstrahlung from plage regions [Felli et al., 1981; Tapping, DeTracey, 1990; Tapping et al., 2003]. Other studies suggest that the index is first affected by a change in the contribution of gyroresonance emission in strong magnetic fields of sunspots in an active region [Schmahl, Kundu, 1995, 1998]. A recent publication [Dudok de Wit et al., 2014] concludes that the gyroresonance emission component may be responsible for 90 % of the index variability. The uncertainty about the causes of the $F10.7$ variability makes it necessary to use not actual values as an index but measurements averaged over tens of days because in this case its correlation with EUV emission becomes higher due to a decrease in the contribution of the non-bremsstrahlung component.

To resolve the ambiguity in the cause of the flux variability, it is necessary to be able to identify the emission of individual sources, i.e. visualization of the solar disk is required. The first attempt to determine the brightness temperature distribution over the quiet solar disk at 2.8 GHz was made by Christiansen and Warburten [1955] during the solar minimum 1952–1954. From one-dimensional scans of the solar disk, near-limb equatorial brightenings and darkenings in the polar regions were found.

Two-dimensional solar disk images at 2.8 GHz were taken only half a century later with the Allen Telescope Array (ATA) [Saint-Hilaire et al., 2012]. The specific difficulty in mapping the solar disk is associated with the need to combine a wide field of view of the telescope (more than 30 arcmin) with a high spatial resolution (~ 10 arcsec). With the ATA resolution of ~ 1.6 arcmin, equatorial near-limb brightenings were clearly observed at 2.8 GHz. Observations at a number of frequencies from 1.43 to 6 GHz in intensity and polarization also made it possible to identify sources of gyroresonance emission. It was concluded that the gyroresonance emission can in some cases make the main contribution to the emission from an active region.

Later, several images of the quiet solar disk with a spatial resolution to 35 arcsec were obtained by the mosaic method from Jansky Very Large Array (VLA) observations. During the observations, there were 11 active regions on the disk. Nonetheless, despite the large number of active regions, the gyroresonance emission contribution to the integral solar emission did not exceed 10 sfu, and the relative contribution to the variable $F10.7$ component was no more than 8 % [Schonfeld et al., 2015].

During the last solar minimum, full solar disk images at six frequencies were published which were obtained using data from the 13-antenna radio interferometer EOVSA, accumulated during daylight hours [Gary et al., 2020; <http://ovsa.njit.edu/SynopticImg/eovsamedia/eovsa-browser>]. The spatial resolution at 3.0 GHz was as high as 20 arcsec and was sufficient for observations of equatorial limb brightenings with brightness temperatures above $50 \cdot 10^3$ K, as well as for identification of bright plage regions and sunspot sources against the background of the disk.

Section 1 discusses SRH characteristics and a method for calibrating brightness temperatures. Section 2 analyzes daily observations at three frequencies in the 3–6 GHz range for 50 days. This section also compares the measured radio maps with the model distributions of brightness radio temperature obtained from AIA/SDO observations of EUV emission. The results are discussed in Section 3 and Conclusion.

1. SIBERIAN RADIO HELIOGRAPH: 3–6 GHz RANGE

The Siberian Radio Heliograph (SRH) is located at the ISTP SB RAS Radio Astrophysical Observatory (RAO) and is designed for regular observations of the Sun in the frequency range 3–24 GHz [Lesovoi et al., 2012; Altyntsev et al., 2020]. From 2021, SRH has been making test observations. In this paper, we have used data from a 3–6 GHz T-shaped array consisting of 129 equidistant antennas of diameter 3 m. We took measurements at frequencies of 2.8, 3.1, 3.4 GHz. Calibration of data, construction and "cleaning" of images are carried out using software developed at ISTP SB RAS, as well as using CASA – standard software for radio interferometric data [CASA Team et al., 2022]. The SRH beam patterns can be represented as ellipses; lengths of their axes are inversely proportional to the frequency, and the orientation angles and dimensions depend on season and local time of observations. In this paper, we discuss observational data acquired from September 1 to October 20, 2021 at times close to local noon. For the measurements, we chose the time around 03 UT without microwave bursts.

Brightness temperatures in SRH images were calibrated by comparing histograms of pixel-to-pixel brightness of the solar disk and the sky. The difference between the histograms' maxima at the given frequency was normalized to the corresponding brightness temperature of the quiet Sun, presented in [Zirin et al., 1991; Borovik et al., 1992]. Regions of the sky were assigned a zero brightness temperature value; and the difference between the histograms' maxima, the quiet Sun's brightness temperature value from [Zirin et al., 1991], obtained for the central part of the quiet solar disk for the corresponding frequency. For 2.8 GHz calibration the maximum of the pixel-to-pixel diagram was assumed to fit a temperature of $27.1 \cdot 10^3$ K; and at frequencies of 3.1 and 3.4 GHz, $24.9 \cdot 10^3$ K and $23.0 \cdot 10^3$ K respectively. We used observations in both circular polarizations (R and L).

The SRH radio maps at 2.8 GHz were compared with those calculated from SDO/AIA EUV emission data. The differential emission measure of each pixel of an image was calculated employing the SPARSE algorithm [Su et al., 2018]. The inputs are EUV maps in six channels (94, 131, 171, 193, 211, 335 Å) for a given moment of time. Brightness temperatures were determined from the differential emission measure, using the library GRFF_DEM_Transfer_64.dll, available at [[https://github.com/kuznetsov-radio/GRFF/tree/master/Bin aries](https://github.com/kuznetsov-radio/GRFF/tree/master/Bin%20aries)] (for details, see [Fleishman et al., 2021]).

2. OBSERVATIONS

We have used a sequence of daily images of the Sun at 2.8, 3.1, 3.4 GHz. The observation period under study began on September 1, 2021, and 50 days corresponded to CR2248 and CR2249. Figure 1 displays solar disk images for the days with the most different integral fluxes: September 17 (top panels, 62.3 sfu) and September 8 (bottom panels, 95.1 sfu). Panels *a*, *e* show magnetograms of the longitudinal magnetic field; on panels *b*, *f* are SRH brightness temperature maps at 2.8 GHz in intensity (R+L); on panels *c*, *g*, masks with areas, where the brightness temperatures $T_{br} > 35 \cdot 10^3$ K, are highlighted in white, and contours indicate areas with the degree of polarization higher than 5%. Panels *d*, *h* present the results of simulation of radio maps at 2.8 GHz according to EUV emission data.

Time profiles of the integral solar fluxes calculated from radio maps are shown in Figure 2. Panel *a* exhibits the $F_{2.8}$ flux and the $F_{10.7}$ time profile, measured at the Canadian Dominion Radio Astrophysical Observatory (DRAO)

[<http://www.wdcb.ru/stp/data/solar.act/flux10.7/daily>].

In terms of the difference in measurement time between DRAO and SRH (~15 hr), the time profiles are similar, but SRH fluxes are systematically underestimated by ~10%. The flux profiles at 3.1 and 3.4 GHz shown in panel *b* are similar to the time dependence of $F_{2.8}$. It is natural to associate the double-humped shape of the profiles with the ~25-day solar rotation. Panel *b* shows the number of active regions and the number of flares got from the SolarMonitor website [<https://www.solarmonitor.org>] for a given day. It is natural to attribute the time variations in $F_{10.7}$ to a change in the number of active regions on the disk. There is no correlation of the $F_{2.8}$ flux with flares

since the fluxes were measured during time periods without flares. Note that there were mainly X-ray C-class flares, except for three X-ray M-class flares on September 23, 2021.

The relationship between flux measurements at DRAO ($F_{10.7}$) and SRH at 2.8, 3.1, and 3.4 GHz is close to linear in the entire range of flux values (Figure 3). Results of the linear correlation between flux densities are shown by solid lines whose slope increases with receiving frequency. The linear correlation coefficient exceeds 0.8 at all the frequencies.

To determine sources of the variations in the integral solar emission flux, compare the radio maps with small and large fluxes obtained during CR 2248 on the days marked in Figure 2 with vertical lines. On the September 17, 2021 map, the near-limb equatorial regions stand out for their brightness (Figure 1, *c*). For numerical estimates henceforward we assume that the radius bounding the near-limb region is 855 arcsec, which is 100 arcsec smaller than the solar radius (white dashed circles). Figure 1, *c* shows that there are also three regions of increased brightness on the disk, whose location corresponds to concentrations of magnetic pores and small sunspots on the magnetogram (Figure 1, *a*), i.e. to plage regions.

Estimated contributions of various sources to integral fluxes are given in Table for the days in the first column. The integral fluxes obtained by integrating brightness temperatures over the entire disk are listed in the second column. The next four columns show increments of the fluxes in bright sources, calculated from the excess of the brightness temperature of each pixel over the calibration value $27.1 \cdot 10^3$ K. Regions with bright sources were identified using the criterion $T_{br} > 35 \cdot 10^3$ K.

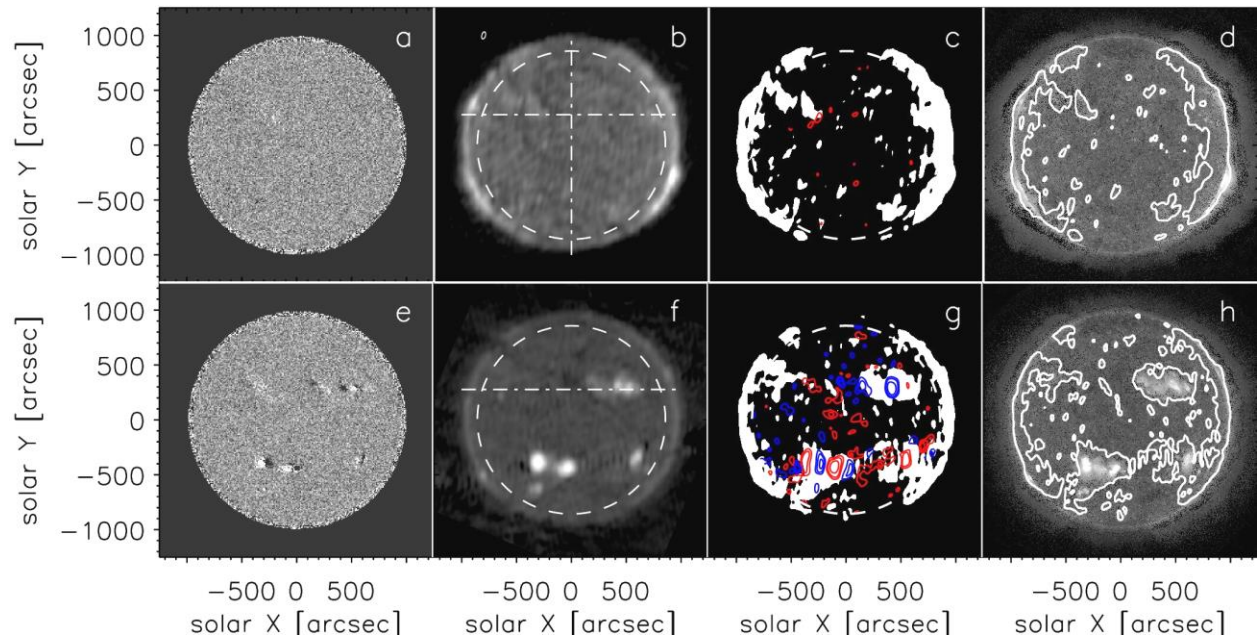


Figure 1. Solar disk images on September 17, 2021 (top panels) and September 8, 2021 (bottom panels): magnetograms of the longitudinal magnetic field (*a*, *e*); SRH brightness temperatures at 2.8 GHz in intensity (*b*, *f*). The white dashed circle bounds a near-limb region. Dash-dot lines indicate the sections used for Figure 4. The SRH beam is in the top left corner. White masks are regions with $T_{br} > 35 \cdot 10^3$ K. The red/blue contours show the degrees of right/left polarization at a level of 0.05 (*c*) and (-0.2, -0.1, -0.05, 0.05, 0.1, 0.2) (*g*); comparison between model (background) and measured brightness temperatures (contours) (*d*, *h*)

Relative contribution of 2.8 GHz emission sources

Date	$F_{2.8}$, sfu	$F_{T_{br}>35\cdot 10^3\text{ K}}$, sfu	F_{limb} , sfu	F_{plage} , sfu	$F_{\text{R-L/R+L}>0.05}$, sfu	F_{DEM} , sfu
08.09	95.1	39.5	4.2	19.2	16.1(40.1 %)	90.0
17.09	62.3	10.0	7.8	2.2	0	71.2
25.09	69.2	16.9	4.0	5.2	7.7(11.1 %)	94.7
27.09	76.7	21.5	7.1	7.8	6.6(8.6 %)	96.5
29.09	87.9	31.3	11.0	14.0	6.3(7.2 %)	106.8

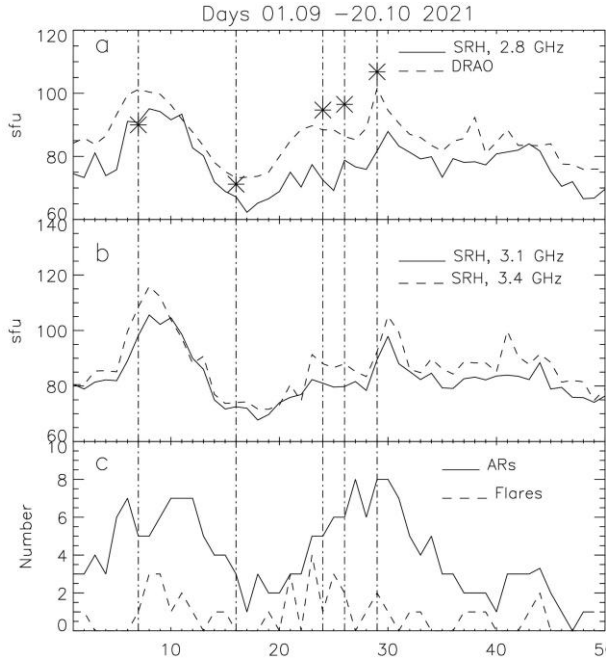


Figure 2. Variations in the integral microwave fluxes of the Sun for 50 days: comparison between $F_{2.8}$ and $F_{10.7}$ fluxes, asterisks mark the results of $F_{10.7}$ calculation from EUV emission maps (a); $F_{3.1}$ and $F_{3.4}$ fluxes (b); the number of active regions and solar flares (c)

On the day with a minimum flux, the increment in all bright regions of the disk is 10 sfu, it is composed of a near-limb brightening with a total flux of 7.8 sfu and additional emission from plage regions of 2.2 sfu. In the last column of Table, the integral solar flux is calculated using a model from EUV emission data.

A large value of the $F_{2.8}$ flux was observed on September 8, 2021, when bright neighborhoods of five active regions appeared on the disk (Figure 1, e, f), above sunspots of which the brightness temperature values exceeded those in quiet solar regions by orders of magnitude, and emission circular polarization degrees were higher than 20 %. In active regions of the southern hemisphere No. 12866 and No. 12868, the maximum brightness temperatures were $2.6 \cdot 10^6$ K and $1.9 \cdot 10^6$ K respectively. On that day, an increase in emission from the regions with increased brightness temperature was equal to 39.5 sfu. At the same time, the area of near-limb brightenings on that day was smaller, and the contribution of their flux decreased to 4.2 sfu. The emission flux from regions with polarization depends on a given degree of polarization. If it is higher than 5 %, the flux is about 16.1 sfu, which is comparable to the increment in the flux from plage regions (19.2 sfu). Thus, an increment in emission at 2.8 GHz with appearance of

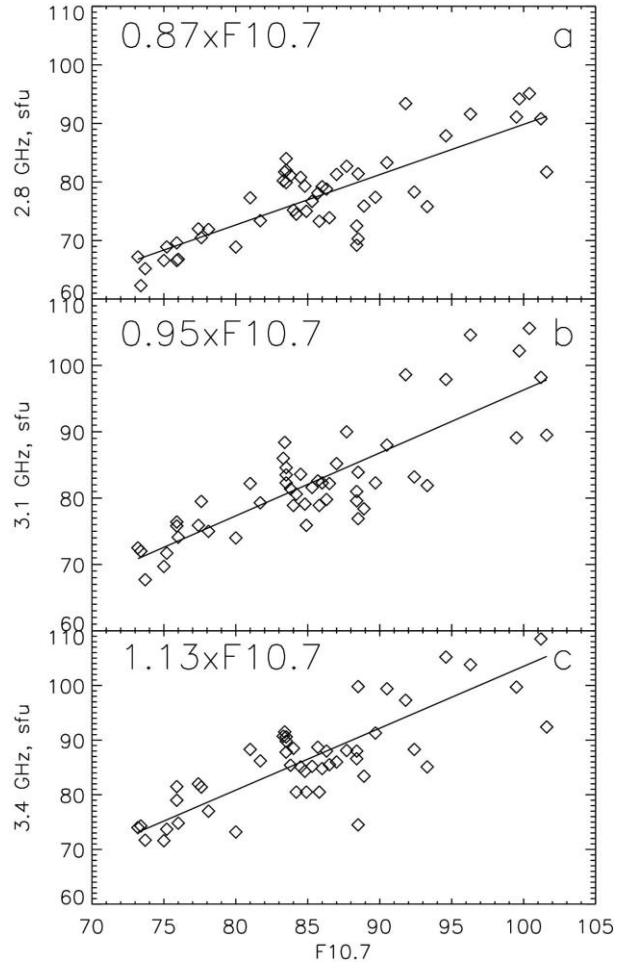


Figure 3. Relationship between flux measurements at DRAO ($F_{10.7}$) and SRH at frequencies of 2.8, 3.1, and 3.4 GHz. Solid lines are linear correlation results

active regions is provided both by the emission from plage regions, located in their vicinity, and by the gyroresonance emission from bright polarized sources above magnetic field spots.

The relative contribution of the September 25, 27, and 29 emission sources during the next rotation CR2249 is shown in Table. On those days there were from five to eight active regions on the disk, but the fluxes from polarized sources remained roughly constant. The contribution of near-limb brightenings varied from 4 to 11 sfu. Especially prominent is September 29 when the contribution of bremsstrahlung from limb and plage regions dominates. Note that when flux increments (third column) are excluded from the total flux (second column) a nearly constant value in the range 52.3–56.7 sfu remains.

On the model maps calculated from EUV emission, especially noticeable are increased brightness regions in the vicinity of active regions (plage regions), close to the radio brightness distribution contours measured with SRH (Figure 1, *d, h*). The integral flux values for five days are marked with asterisks in Figure 2 and are given in the last column of Table. To compare the absolute values of measured and model brightnesses, examine them along the sections indicated by dashed lines in Figure 1, *b, f*.

Figure 4, *a–c* illustrates the brightness temperature distribution in intensity at three frequencies and in polarization at 2.8 GHz along sections of the disk. Dotted and dashed lines indicate the brightness temperature levels $2.7 \cdot 10^4$ K and $3.5 \cdot 10^4$ K respectively. The first line shows the temperature used for calibration by the method of histograms; the second, the level over radio brightness fluctuations used to highlight the increased brightness regions displayed in Figure 1. The similarity between the brightness temperature profiles at the three frequencies suggests that the level of fluctuations of non-solar origin does not exceed 10^3 K. Note that the contribution of near-limb brightenings decreases with an increase in the receiving frequency.

Panels *d, e* exhibit sections of measured and model brightness temperature distributions at 2.8 GHz. The model profile is smoothed with a window of width 35 arcsec, close to the size of the SRH beam pattern at this frequency. Comparing these profiles shows that the excess of the model flux by 14 % may be associated with the large contribution of equatorial near-limb regions. The brightness temperature distribution along the central meridian (Figure 4, *b, e*) is close to flat and does not exhibit increased emission in the circumpolar region.

In the case of active regions, the section passes through active regions No. 12864 and No. 12865 whose radio brightness is as high as $6 \cdot 10^5$ K (Figure 4, *c, f*). In the active region, a source with polarization up to 30 % stands out in which a change in the temperature ratio is

also observed in the range 2.8–3.4 GHz. In the model profile calculated from EUV data, this source is matched by a dip in intensity. At the same time, the highest brightness peaks in the model and measured profiles are close in place and amplitude.

3. DISCUSSION

Comparing the time dependences of solar emission fluxes obtained by integrating two-dimensional radio brightness distributions with fluxes measured at high accuracy at DRAO demonstrates their similarity. The cross-correlation coefficient is 0.87, and the delay of ~ 18 hrs is consistent with the difference in the measurement time between RAO and DRAO in Canada. At the same time, the fluxes received by SRH at 2.8 GHz are systematically underestimated relative to the Canadian data by ~ 10 % (Figure 2, *a*).

The systematic error in calibrating brightness temperatures in SRH images may appear for two reasons. The first refers to the error in determining the instrumental value of the quiet Sun's brightness from the maximum of the histogram of pixel-to-pixel signals. The linear dependence of the flux measured by SRH at 2.8 GHz on DRAO data excludes the influence of nonlinearity of brightness measurements. The radio brightness profile along the pole-to-pole section without crossing plage regions and limb brightenings is flat; this suggests that the large-scale image distortions characteristic of interferometers, such as field slopes, depressions near the disk center, do not significantly affect the position of the histogram maximum (Figure 4, *b, e*). A more likely reason for the systematic underestimation of brightness temperature is the difference of the actual temperature of the quiet solar regions outside active regions from the value used in calibration, which was obtained in [Zirin et al., 1991; Borovik et al., 1992]. This value $27.1 \cdot 10^3$ K was derived in both works during the solar minimum between cycles 20 and 21. Note that

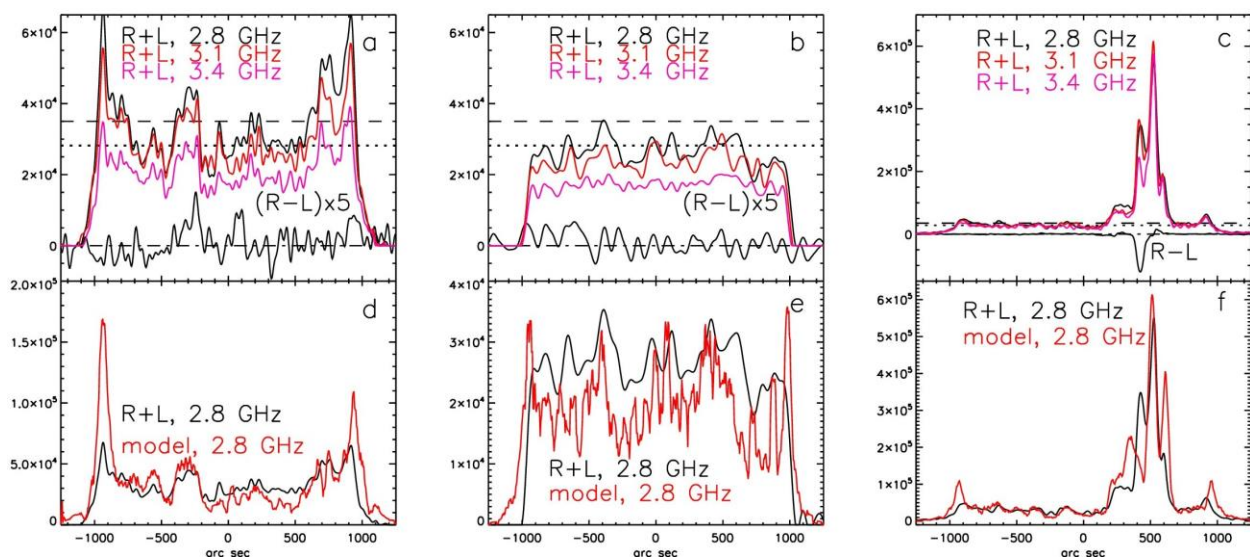


Figure 4. Brightness temperature distribution in intensity at three frequencies, R–L polarization (panels *a–c*) and model profile according to EUV emission data (panels *d–f*) at 2.8 GHz along the disk sections shown in Figure 1. Along the Y-axis are brightness temperatures in kelvins. Panels *a, d* — September 17, latitudinal section. The R–L flux is scaled up 5 times. Panels *b, e* — September 17, meridional section. Panels *c, f* — similar relationships for September 8

even at solar minimum the contribution of optically thin coronal emission, which can vary during the cycle and between them, is ~15 sfu [Schonfeld et al., 2015]. In our case, without active regions, the contribution of coronal emission only in near-limb and plage regions is 10 sfu. Evidence for the variability of the quiet solar flux can also be found in [Tapping, Valdes, 2011].

SRH observations in intensity and polarization can identify bremsstrahlung and gyroresonance components in the integral emission from the quiet Sun in real time (see Table). The main contribution to the optically thin emission is made by bremsstrahlung. On the other hand, in terms of the contribution of different mechanisms to the integral flux variability, the relative contributions of bremsstrahlung and gyroresonance emissions can be comparable in value. The contribution of equatorial near-limb brightenings to the variability is relatively small and amounts to ~5 sfu. The flux variations are linked with active regions on the disk. Bremsstrahlung is generated in plage regions in the vicinity of active regions. Gyroresonance emission with brightness up to several MK is generated in strong magnetic fields above sunspots, but their contribution is rather small due to the small size of the sources.

CONCLUSION

Test observations at the Siberian Radio Heliograph have made it possible for the first time to obtain a sequence of solar disk images in intensity and polarization at several frequencies, including 2.8 GHz. By comparing the total flux time profiles calculated from SRH images with DRAO data, we have tested a method for calibrating the radio brightness of images, using the tabular data obtained in [Zirin et al., 1991; Borovik et al., 1992] during a solar minimum. With a high cross-correlation, we have found out that the fluxes measured by SRH are systematically underestimated, which may suggest that the brightness temperature of the quiet Sun varies outside active regions in the solar activity cycle. Analysis of the SRH images in intensity and polarization has shown that the main contribution to emission is provided by optically thick emission of the chromosphere and bremsstrahlung of the lower corona. The emission variability is determined by variations in emission from plage regions in the vicinity of active regions and gyroresonance emission from polarized sources above sunspots. The commissioning of SRH will allow regular monitoring of the proxy index $F10.7$ with identification of the bremsstrahlung component in real time.

The work was financially supported by RSF (Grant No. 22-22-00019). We are grateful to the RAO, SDO, and DRAO teams for open access to data. The experimental data were obtained using the Unique Research Facility Siberian Solar Radio Telescope [<https://ckp-rf.ru/catalog/usu/73606/>].

REFERENCE

Altyntsev A.T., Lesovoi S.V., Globa M.V., Gubin A.V., Kochanov A.A., Grechnev V.V., Ivanov E.F., et al. Multiwave Siberian Radioheliograph. *SolarTerrestrial Physics*. 2020, vol. 6, iss. 2, pp. 30–40. DOI: [10.12737/stp62202003](https://doi.org/10.12737/stp62202003).

Bilitza D., Reinisch B.W. International Reference Ionosphere 2007: Improvements and new parameters. *Adv. Space Res.* 2008, vol. 42, iss. 4, pp. 599–609. DOI: [10.1016/j.asr.2007.07.048](https://doi.org/10.1016/j.asr.2007.07.048).

Borovik V.N., Kurbanov M.S., Makarov V.V. Distribution of radio brightness of the quiet Sun in the 2-centimeter to 32-centimeter range. *Soviet Astronomy*. 1992, vol. 36, pp. 656.

CASA Team, Bean B., Bhatnagar S., et al. CASA, the Common Astronomy Software Applications for radio astronomy. *Publications of the Astronomical Society of the Pacific*. 2022, vol. 134, iss. 1041, id. 114501, 17 p. DOI: [10.1088/1538-3873/ac9642](https://doi.org/10.1088/1538-3873/ac9642).

Christiansen W.N., Warburton J.A. The distribution of radio brightness over the solar disk at a wavelength of 21 centimetres. III. The quiet Sun two-dimensional observations. *Australian J. Phys.* 1955, vol. 8, pp. 474. DOI: [10.1071/PH550474](https://doi.org/10.1071/PH550474).

Covington A.E. Solar radio emission at 10.7 cm, 1947–1968. *J. Royal Astron. Society of Canada*. 1969, vol. 63, pp. 125.

Dudok de Wit T., Bruinsma S., Shibasaki K. Synoptic radio observations as proxies for upper atmosphere modelling. *J. Space Weather and Space Climate*. 2014, vol. 4, id. A106, 13 p. DOI: [10.1051/swsc/2014003](https://doi.org/10.1051/swsc/2014003).

Felli M., Lang K.R., Willson R.F. VLA observations of solar active regions. I. The slowly varying component. *Astrophys. J.* 1981, vol. 247, pp. 325–347. DOI: [10.1086/159041](https://doi.org/10.1086/159041).

Fleishman G.D., Kuznetsov A.A., Landi E. Gyroresonance and free-free radio emissions from multithermal multicomponent plasma. *Astrophys. J.* 2021, vol. 914, iss. 1, id. 52, 16 p. DOI: [10.3847/1538-4357/abf92c](https://doi.org/10.3847/1538-4357/abf92c).

Gary D., Yu S., Chen B., LaVilla V. A new view of the solar atmosphere: daily full-disk multifrequency radio images from AEOVSA. *American Astronomical Society Meeting Abstracts*. 2020, vol. 235, p. 385.0.

Jacchia L.G. Revised Static Models of the thermosphere and exosphere with empirical temperature profiles. *SAO Special Repp.* 1971, vol. 332.

Krueger A. Introduction to Solar Radio Astronomy and Radio Physics. 1979, 330 p.

Kundu M.R. Solar Radio Astronomy. 1965.

Lesovoi S.V., Altyntsev A.T., Ivanov E.F., Gubin A.V. The multifrequency Siberian Radioheliograph. *Solar Phys.* 2012, vol. 280, iss. 2, pp. 651–661. DOI: [10.1007/s11207-012-0008-7](https://doi.org/10.1007/s11207-012-0008-7).

Saint-Hilaire P.P., Hurford G.J., Keating G., et al. Allen Telescope Array multi-frequency observations of the Sun. *Solar Phys.* 2012, vol. 277, iss. 2, pp. 431–445. DOI: [10.1007/s11207-011-9906-3](https://doi.org/10.1007/s11207-011-9906-3).

Schmahl E.J., Kundu M.R. Microwave proxies for sunspot blocking and total irradiance. *J. Geophys. Res.* 1995, vol. 100, no. A10, pp. 19851–19864. DOI: [10.1029/95JA00677](https://doi.org/10.1029/95JA00677).

Schmahl E.J., Kundu M.R. Synoptic Radio Observations. *Synoptic Solar Physics*. 1998, vol. 140, p. 387.

Schonfeld S.J., White S.M., Henney C.J., et al. Coronal sources of the solar $F10.7$ radio flux. *Astrophys. J.* 2015, vol. 808, iss. 1, id. 29, 10 p. DOI: [10.1088/0004-637X/808/1/29](https://doi.org/10.1088/0004-637X/808/1/29).

Schonfeld S.J., White S.M., Hock-Mysliwiec R.A., McAteer R.T.J. The slowly varying corona. I. Daily differential emission measure distributions derived from EVE spectra. *Astrophys. J.* 2017, vol. 844, iss. 2, article id. 163, 16 p. DOI: [10.3847/1538-4357/aa7b35](https://doi.org/10.3847/1538-4357/aa7b35).

Su Y., Veronig A.M., Hannah I.G., et al. Determination of differential emission measure from solar extreme ultraviolet images. *Astrophys. J.* 2018, vol. 856, iss. 1, article id. L17, 10 p. DOI: [10.3847/2041-8213/aab436](https://doi.org/10.3847/2041-8213/aab436).

Swarup G., Kakinuma T., Covington A.E., et al. High-resolution studies of ten solar active regions at wavelengths of 3–21 cm. *Astrophys. J.* 1963, vol. 137, p. 1251. DOI: [10.1086/147601](https://doi.org/10.1086/147601).

Tapping K.F. Recent solar radio astronomy at centimeter wavelengths: the temporal variability of the 10.7-cm flux. *J. Geophys. Res.* 1987, vol. 92, pp. 829–838. DOI: [10.1029/JD092iD01p00829](https://doi.org/10.1029/JD092iD01p00829).

Tapping K.F., DeTracey B. The origin of the 10.7-cm flux. *Solar Phys.* 1990, vol. 127, iss. 2, pp. 321–332. DOI: [10.1007/BF00152171](https://doi.org/10.1007/BF00152171).

Tapping K.F., Valdés J.J. Did the Sun change its behaviour during the decline of cycle 23 and into cycle 24? *Solar Phys.* 2011, vol. 272, iss. 2, article id. 337. DOI: [10.1007/s11207-011-9827-1](https://doi.org/10.1007/s11207-011-9827-1).

Tapping K.F., Cameron H.T., Willis A.G. S-component sources at 21 cm wavelength in the rising phase of cycle 23. *Solar Phys.* 2003, vol. 215, iss. 2, pp. 357–383. DOI: [10.1023/A:1025645908639](https://doi.org/10.1023/A:1025645908639).

Tobiska W.K., Bouwer S.D., Bowman B.R. The development of new solar indices for use in thermospheric density modeling. *J. Atmos. Solar-Terr. Phys.* 2008, vol. 70, iss. 5, pp. 803–819. DOI: [10.1016/j.jastpp.2007.11.001](https://doi.org/10.1016/j.jastpp.2007.11.001).

Zirin H., Baumert B.M., Hurford G.J. The microwave brightness temperature spectrum of the quiet Sun. *Astrophys. J.* 1991, vol. 370, p. 779. DOI: [10.1086/169861](https://doi.org/10.1086/169861).

URL: <http://ovsa.njit.edu/SynopticImg/eovsamedia/eovsaw-browser> (assessed February 25, 2023).

URL: <https://github.com/kuznetsov-radio/GRFF/tree/master/Binaries> (assessed February 25, 2023).

URL: <http://www.wdcb.ru/stp/data/solar.act/flux10.7/daily> (assessed February 25, 2023).

URL: <https://www.solarmonitor.org> (assessed February 25, 2023).

URL: <https://ckp-rf.ru/catalog/usu/73606/> (assessed February 25, 2023).

This paper is based on material presented at the 18th Annual Conference on Plasma Physics in the Solar System, February 6–10, 2023, IKI RAS, Moscow.

Original Russian version: Altyntsev A.T., Globa M.V., Meshalkina N.S., published in *Solnechno-zemnaya fizika*. 2023. Vol. 9. Iss. 2. P. 71–77. DOI: [10.12737/szf-92202308](https://doi.org/10.12737/szf-92202308). © 2023 INFRA-M Academic Publishing House (Nauchno-Izdatelskii Tsentr INFRA-M)

How to cite this article

Altyntsev A.T., Globa M.V., Meshalkina N.S. Quiet solar corona: daily images at 8.8–10.7 cm wavelengths. *Solar-Terrestrial Physics*. 2023. Vol. 9. Iss. 2. P. 66–72. DOI: [10.12737/stp-92202308](https://doi.org/10.12737/stp-92202308).